Dalton Transactions

An international journal of inorganic chemistry

Accepted Manuscript

This article can be cited before page numbers have been issued, to do this please use: J. Goura, P. Halder, N. Barman, S. Mukhopadhyay, B. Schwarz, S. K. Singh and I. Tarannum, *Dalton Trans.*, 2025, DOI: 10.1039/D4DT02976C.

ROYAL SOCIETY OF CHEMISTRY

rsc.li/dalton

View Article Online
DOI: 10.1039/D4DT02976C

Tetranuclear $\{Ln^{III}\}_4$ Complexes Possessing Homometallic *O-Capped* Structural Subunits: Study of Magnetic and Photoluminescent Properties

Purbashree Halder[a], Nandini Barman[a], Ibtesham Tarannum,[c] Subrata Mukhopadhyay[a], Björn Schwarz[b], Saurabh Kumar Singh[c]* and Joydeb Goura*[a,d,e]*

[a]Department of Chemistry, Jadavpur University, Kolkata-700032, India

[b]Karlsruhe Institute of Technology (KIT) – Institute for Applied Materials (IAM), Hermann-von-Helmholtz-Platz 1, 76344 Eggenstein-Leopoldshafen, Germany

[c]Computational Inorganic Chemistry Group, Department of Chemistry, Indian Institute of Technology Hyderabad, Kandi, Sangareddy, Telangana-502284, India

[d]Department of Chemistry, University of Delhi, Delhi-110007, India

[e]Department of Chemistry, Bangabasi College, Kolkata-700009, West Bengal, India

E-Mail: jgoura@chemistry.du.ac.in
joydebgoura@gmail.com
bjoern.schwarz@kit.edu
sksingh@chy.iith.ac.in

View Article Online
DOI: 10.1039/D4DT02976C

Abstract

A series of homometallic tetranuclear Ln_4 complexes, $[Ln_4(\mu_3\text{-}OH)_2\{py_2C(OH)O\}_2(O_2CCMe_3)_8]$ [$\{py_2C(OH)O\}^-$ = monoanionic *gem*-diol form of di-2-pyridyl ketone; Ln = Nd (**1**), Eu (**2**), Tb (**3**), Dy (**4**), Er (**5**) and Yb (**6**)] have been synthesized and characterized. The asymmetric unit of each of the tetranuclear derivatives comprises the dinuclear motif, $[Ln_2(\mu_3\text{-}OH)\{py_2C(OH)O\}(O_2CCMe_3)_4]$. The core structure of this Ln_4 family possesses two homometallic *O-capped* structural subunits, Ln^{III}_3O which are further connected through the bridging μ_3-OH ligands. Mean plane analysis indicates that all the lanthanide centers lie in the same plane. There are two types of eight-coordinated lanthanide centers present. The shape analysis revealed that the Ln1 center possesses a distorted elongated trigonal bipyramidal geometry while the Ln2 center has a distorted Johnson elongated triangular bipyramidal geometry. The solid-state room temperature photoluminescence studies of **1**-**5** show the ligand center emission band at 306 nm when excited at 270 nm. Compound **1**, when excited at 380 nm emits at 517, 624, and 724 nm. On the other hand, excitation at 360 nm of compound **3**, leads to emission peaks at 489, 542, 583, 590, and 624 nm. These bands are due to the Ln(III) centers *f-f* transitions. Direct current (DC) and alternating current (AC) magnetization were measured in dependence of temperature and magnetic field, for all complexes. Magnetic anisotropy and magnetic relaxation mechanism were also studied using complete active space self-consistent field CASSCF) methodology for **1**-**6** complexes. The SINGLE_ANISO module is used to extract the relevant spin-Hamiltonian parameters for all the complexes. We have calculated the magnetic exchange couplings (J_1–J_3) for all the complexes. For complexes **3** and **4**, we observed a sizable tunnel splitting of 1.5×10^{-3} cm^{-1} and $1.9 \times 10^{-3} cm^{-1}$, indicating that QTM is still a dominant mechanism for magnetic relaxation in the exchange-coupled systems, resulting in diminishing the SMM behaviour.

View Article Online
DOI: 10.1039/D4DT02976C

Keywords: Di-2-pyridyl ketone; Pivalate; 4f complexes; *O-capped* cluster, magnetic susceptibility; Luminescence

Introduction

Multi-dentate coordinating organic and inorganic ligands have been extensively used for developing lanthanide ions-based single-molecule magnets (SMMs).[1] Among them, the di-2-pyridyl ketone, $(py)_2CO$ has ubiquitous coordination capabilities, since it contains hetero-donor sites including one oxygen and two nitrogen atoms. The neutral $(py)_2CO$ can act as a bidentate chelating ligand, while tri- or tetra-dentate behavior has been observed for geminal diol form which formed in the presence of a base. The $(py)_2CO$ has a strong coordination binding capability towards soft and hard metal ions. In addition, two pyridine groups attached to the carbonyl slightly enhance the electrophilicity nature of the carbonyl group. As a result, the hemiketal formation is faster in the presence of solvents (such as H_2O, MeOH, EtOH, etc.) (**Chart 1**).[2] The hemiketal ligand has beneficial properties for binding the oxophilic lanthanide ions. On the other hand, the hydrazine derivative of the $(py)_2CO$ ligand shows strong fluorescence properties in an acidic medium.[3]

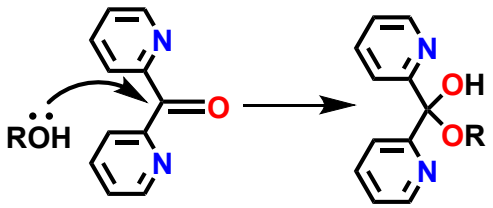

R = H, Me, Et etc

Chart 1. Hemiketal form of di-2-pyridyl ketone.

Therefore, the neutral $(py)_2CO$ has the potential ability to assemble the polynuclear lanthanide complexes. Polymetallic lanthanide complexes have captivated great interest for the last few decades owing to their potential applications in modern molecular qubits,[4] molecular spintronics,[5] quantum computations,[6] magnetic refrigeration,[7] photochromic materials,[8] and

View Article Online
DOI: 10.1039/D4DT02976C

particularly for single-molecule-magnets (SMMs).[1] SMM properties have been extensively studied for polynuclear lanthanide complexes due to their high ground spin state (*S*) and Tb(III),[9] Dy(III),[10] Ho(III),[11] and Er(III)[12] ions show strong magnetic anisotropy (*D*). However, achieving a high spin ground state by ferromagnetic coupling between the lanthanide ions is very challenging. Simultaneously, the blocking temperature is another key factor in controlling SMM behavior that is certainly determined by the magnetic anisotropy, caused by the zero-field splitting (ZFS).[13] A pure uniaxial negative ZFS parameter *D* is desirable for a good SMM characteristic with slow magnetic spin-lattice relaxation and long conservation of the magnetic Ising limit.[13] The high uniaxial anisotropy possesses a large energy barrier, U_{eff} with accompanying high blocking temperature for reversal magnetization .[14]

An effective energy barrier that ensures slow spin-lattice relaxation strongly depends on the coordination environment and the geometry around the Ln(III) ion.[15] The electronic and steric factors of the ligands have a crucial role in determining the geometry and control of the magnetic properties. The literature survey revealed that varieties of polynuclear lanthanide complexes are reported such as di-, tri-, tetra-, penta-, hexa, and higher nuclearities.[16] Among them, the tetranuclear derivatives got much attention owing to their structural arrangements [*e.g.* rhombus shape, cubane, butterfly, square, rectangle, chainlike, linear, Y-shape, see-saw, zigzag irregular shape, and square grids (2 × 2), etc.] and magnetic behavior depending on the organic ligand backbone.[16] So, the proper design of the organic ligands can regulate the structural patterns and coordination numbers which can modulate the coordination geometry and magnetic properties. The varieties of tetranuclear lanthanide derivatives have been reported based on several organic and inorganic ligands.[16] Indeed, the neutral $(py)_2CO$ as primary ligand-based tetranuclear lanthanide complexes have not been reported yet.

In this regard, the $(py)_2CO$ ligand is of great interest for assembling tetranuclear lanthanide complexes due to its multidentate nature as well as control of the magnetic and

View Article Online
DOI: 10.1039/D4DT02976C

photoluminescent properties. Accordingly, herein we report a series of tetranuclear homometallic *O-capped* lanthanide complexes **1-6** based $(py)_2CO$ ligand. Detailed magnetic and luminescence studies have been investigated.

Experimental

Reagents and general procedures

Solvents and other general reagents used in this work were purified according to standard procedures.[17] Di-2-pyridylketone $(py)_2CO$ and Sodium Pivalate Hydrate (NaPiv) from TCI, NEt_3 (S.D fine), $NdCl_3 \cdot 6H_2O$, $EuCl_3 \cdot 6H_2O$, $ErCl_3 \cdot 6H_2O$, $YbCl_3 \cdot 6H_2O$ from Alfa Aesar, $TbCl_3 \cdot 6H_2O$ from SRL and $DyCl_3 \cdot 6H_2O$ from Sigma-Aldrich were obtained and used as received.

Instrumentation

Melting points were measured using a JSGW melting point apparatus and the presented values are uncorrected. Fourier transform infrared (FT-IR) spectra were recorded with a PerkinElmer LX-1 FT-IR spectrophotometer (4000–400 cm^{-1}) by using a modern diamond attenuated total reflectance (ATR) accessory. Elemental analyses of the compounds were performed using a PerkinElmer 2400 Series-II CHN analyzer. The solid-state emission spectra were recorded on a Perkin-Elmer-Lambda 20 spectro photometer.

X-ray Crystallography

Single-crystal X-ray structural studies of **1–6** were performed on a *Bruker SMART APEX* CCD diffractometer. Data were collected using a graphite-monochromated MoK_α radiation (λ = 0.71073 Å). The crystals did not degrade/decompose during the data collection. Data collection, structure solution, and refinement were performed using the *SMART, SAINT* and *SHELXTL* programs, respectively.[18a-f] All of the non-hydrogen atoms were refined anisotropically using full-matrix least-square procedures. All of the hydrogen atoms were fixed

View Article Online
DOI: 10.1039/D4DT02976C

at idealized positions and a riding model was used. All of the mean plane analyses and molecular drawings were obtained using Diamond (version 3.1).

DC and AC Magnetometry

Direct current (DC) and alternating current (AC) magnetometry were measured using a Physical Property Measurement System (PPMS) DynaCool from Quantum Design equipped with an ACMS-II option. The powder complexes of **1** (Nd), **2** (Eu), **3** (Tb), **4** (Dy), **5** (Er), and **6** (Yb), were used to measure DC magnetomety. The sample powders were filled into gelatin capsules (QDC-AGC1 from Quantum Design) and were mechanically fixed with Icosane (about 50 mg) to prevent particle reorientation. The capsules were fixed with some polyimide tape within magnetically neutral sample holder straws (QDS-8000-001 from Quantum Design) and attached to the sample holder rod. DC magnetization vs. temperature was measured at a magnetic field of 1000 Oe from 2 K to 50 K in settle mode and from 51 K to 200 K in sweep mode with a 1 K/min heating rate. The temperature step size for signal acquisition was 1 K with a signal averaging time of 10 seconds. Magnetization vs. field was measured at 2, 5, 10, 15, 20, 25, 35, 50, and 300 K up to 7 T (complexes **3** and **4** were not measured at 300 K) with a signal averaging time of 10 seconds and a three-fold redundancy per measuring point. Due to the strong magnetic signal stemming from the lanthanoids, no corrections for diamagnetic contributions have been done. AC susceptibility was measured from 50 Hz to 10 kHz at 27 different frequencies with a log-distribution at 2 K at various magnetic DC fields, as indicated in the corresponding figures (maximum field was 2500 Oe). The AC excitation field was 5 Oe with an average time per measuring point of 10 seconds.

Synthesis

General procedure for the synthesis of 1–6

The following general protocol was utilized for the synthesis of homometallic tetranuclear lanthanide complexes. $LnCl_3 \cdot 6H_2O$ was added to a stirred solution of di-2-pyridyl ketone

View Article Online
DOI: 10.1039/D4DT02976C

$(py)_2CO$ in methanol (20 mL). To this solution, sodium pivalate (NaPiv) hydrate and triethylamine (NEt_3) were added. The solution was stirred for 30 minutes at 60°C, affording a clear colorless solution. This solution was evaporated in a rotary evaporator to dry, re-dissolve in methanol, and filtered. The filtrate was allowed to evaporate slowly at room temperature. After two weeks, colorless crystals suitable for X-ray diffraction have formed. Specific quantities of the reactants involved in each reaction, yields of the products, and their characterization data are given below.

$[Nd_4(\mu_3\text{-}OH)_2\{py_2C(OH)O\}_2(O_2CCMe_3)_8]$ (1)

Quantities: $(py)_2CO$ (0.062 g, 0.336 mmol), $NdCl_3 \cdot 6H_2O$ (0.060 g, 0.168 mmol), NEt_3 (0.4 mL, 2.869 mmol), NaPiv (0.072 g, 0.507 mmol). Yield: 0.046 g, 53 % (based on Nd). Mp: 200 °C (d). IR (KBr) (cm^{-1}): 3362(br), 2961(br), 1514(w), 1482(s), 1415(s), 1374(w), 1226(m), 1147(m), 1088(m), 1064(s), 1043(w), 1011(m), 938(w), 896(m), 846(m), 812(s), 790(m), 758(s), 631(m), 593(s), 593(m), 400(s). Anal. calcd for $C_{62}H_{92}N_4Nd_4O_{22}$ (1822.39): C, 40.86; H, 5.09; N, 3.07. Found: C, 39.61; H, 4.88; N, 2.93.

$[Eu_4(\mu_3\text{-}OH)_2\{py_2C(OH)O\}_2(O_2CCMe_3)_8]$ (2)

Quantities: $(py)_2CO$ (0.061 g, 0.336 mmol), $EuCl_3 \cdot 5H_2O$ (0.062 g, 0.168 mmol), NEt_3 (0.4 mL, 2.869 mmol), NaPiv (0.072 g, 0.507 mmol). Yield: 0.041 g, 50 % (based on Eu). Mp: 200 °C (d). IR (KBr) (cm^{-1}) 2963(br), 1579(w), 1521(w), 1485(s), 1425(s), 1378(w), 1362(s), 1227(m), 1166(m), 1038(m), 1014(w), 943(w), 898(m), 807(m), 759(s), 671(s), 631(m), 596(s), 403(s). Anal. calcd for $C_{62}H_{92}Eu_4N_4O_{22}$ (1853.28): C, 40.18; H, 5.00; N, 3.02. Found: C, 39.92; H, 4.81; N, 2.86.

$[Tb_4(\mu_3\text{-}OH)_2\{py_2C(OH)O\}_2(O_2CCMe_3)_8]$ (3)

Quantities: $(py)_2CO$ (0.062 g, 0.336 mmol), $TbCl_3 \cdot 5H_2O$ (0.063 g, 0.168 mmol), NEt_3 (0.4 mL, 2.869 mmol), NaPiv (0.072 g, 0.507 mmol). Yield: 0.040 g, 51 % (based on Tb). Mp: 200 °C (d). IR (KBr) (cm^{-1}): 2961(br), 1567(w), 1516(w), 1485(s), 1424(s), 1377(w), 1297(w),

View Article Online
DOI: 10.1039/D4DT02976C

1227(m), 1209(m), 1117(m), 1164(s), 1079(m), 1079(m), 1039(w), 943(w), 896(m), 817(m), 808(m), 791(m), 759(s), 670(s), 649(m), 632(m), 595(s), 564(m), 400(s). Anal. calcd for $C_{62}H_{92}Tb_4N_4O_{22}$ (1881.13): C, 39.59; H, 4.93; N, 2.98. Found: C, 39.32; H, 4.74; N, 2.83

$[Dy_4(\mu_3\text{-}OH)_2\{py_2C(OH)O\}_2(O_2CCMe_3)_8]$ (4)

Quantities: $(py)_2CO$ (0.062 g, 0.336 mmol), $DyCl_3 \cdot 5H_2O$ (0.064 g, 0.168 mmol), NEt_3 (0.4 mL, 2.869 mmol), NaPiv (0.072 g, 0.507 mmol). Yield: 0.042 g, 52 % (based on Dy). Mp: 200 °C (d). IR (KBr) (cm^{-1}): 2981(br), 1577(w), 1517(w), 1485(s), 1424(s), 1377(w), 1297(w), 1227(m), 1210(m), 1114(m), 1137(s), 1079(m), 1014(w), 943(w), 826(m), 816(m), 791(m), 758(s), 670(s), 658(w), 649(m), 632(m), 596(s), 565(m), 532(m), 400(s). Anal. calcd for $C_{62}H_{92}Dy_4N_4O_{22}$ (1895.42): C, 39.29; H, 4.89; N, 2.96. Found: C, 39.04; H, 4.69; N, 2.82.

$[Er_4(\mu_3\text{-}OH)_2\{py_2C(OH)O\}_2(O_2CCMe_3)_8]$ (5)

Quantities: $(py)_2CO$ (0.062 g, 0.336 mmol), $ErCl_3 \cdot 5H_2O$ (0.065 g, 0.168 mmol), NEt_3 (0.4 mL, 2.869 mmol), NaPiv (0.072 g, 0.507 mmol). Yield: 0.040 g, 50 % (based on Er). Mp: 200 °C (d). IR (KBr) (cm^{-1}): 2961(br), 1579(w), 1519(w), 1460(s), 1426(s), 1378(w), 1297(w), 1228(m), 1212(m), 1167(m), 1150(m), 1080(s), 1037(w), 944(w), 898(m), 809(m), 791(m), 671(s), 650(w), 650(m), 632(m), 598(s), 567(m), 534(m), 400(s). Anal. calcd for $C_{62}H_{92}Er_4N_4O_{22}$ (1914.46): C, 38.90; H, 4.84; N, 2.93. Found: C, 38.66; H, 4.62; N, 2.79.

$[Yb_4(\mu_3\text{-}OH)_2\{py_2C(OH)O\}_2(O_2CCMe_3)_8]$ (6)

Quantities: $(py)_2CO$ (0.062 g, 0.33 mmol), $YbCl_3 \cdot 5H_2O$ (0.066 g, 0.168 mmol), NEt_3 (0.4 mL, 2.869 mmol), NaPiv (0.072 g, 0.507 mmol). Yield: 0.040 g, 50 % (based on Er). Mp: 200 °C (d). IR (KBr) (cm^{-1}): 2961(br), 1579(w), 1519(w), 1460(s), 1426(s), 1378(w), 1297(w), 1228(m), 1212(m), 1167(m), 1150(m), 1080(s), 1037(w), 944(w), 898(m), 809(m), 791(m), 671(s), 650(w), 650(m), 632(m), 598(s), 567(m), 534(m), 400(s). Anal. calcd for $C_{62}H_{92}Yb_4N_4O_{22}$ (1937.64): C, 38.43; H, 4.79; N, 2.89. Found: C, 38.19; H, 4.58; N, 2.77.

View Article Online
DOI: 10.1039/D4DT02976C

Results and Discussion

Synthesis

The utility of di-2-pyridyl ketone, $(py)_2CO$ as a ligand has been pioneered, among others, by Spyros P. Perlepes and his research group.[2,19] Most of this work pertains to compounds that possess 3d or 3d/4f based magnetic clusters.[2,19] The interesting phenomenon of the $(py)_2CO$ ligand is that the coordination binding modes can be fine-tuned depending on the reaction medium (*i.e*. neutral or germinal diol systems) (*vide supra*) (**Chart 1**).[2,19] The multi-dentate nature of $(py)_2CO$ is the potential for the assembling of tetranuclear lanthanide magnetic ensembles. In addition, the NaPiv ligand plays a cluster-expanding agent for the formation of the tetranuclear lanthanide complexes. Therefore, in the reaction of lanthanide salts with $(py)_2CO$, NaPiv in the presence of NEt_3 as a base afforded a series of tetranuclear homometallic lanthanide complexes **1-6**, the general formula is $[Ln_4(\mu_3\text{-}OH)_2\{py_2C(OH)O\}_2(O_2CCMe_3)_8]$ (**Scheme 1**). Compounds **1-6** have been characterized by various physicochemical methods such as IR, X-ray single crystals, magnetic, and luminescence studies. The IR spectra of compounds **1-6** exhibit a medium intensity band at 2961 cm^{-1}, which is assigned to the ν(OH) stretching vibration of the $[(py)_2C(OH)O]^-$ ligand. It shows bands at 1577 cm^{-1} due to the formation of the metal complex via in situ generated germinal diol of $(py)_2CO$ ligand[20] [free carbonyl stretching vibration band of $(py)_2CO$ is ν(C=O), at 1684 cm^{-1}].[20] The bands at 1037 cm^{-1}, 758 cm^{-1}, and 594 cm^{-1} are attributed to out-of-plane bending stretching vibration of pyridyl C-H bonds and in-plane pyridyl ring deformation vibration respectively.[20]

View Article Online
DOI: 10.1039/D4DT02976C

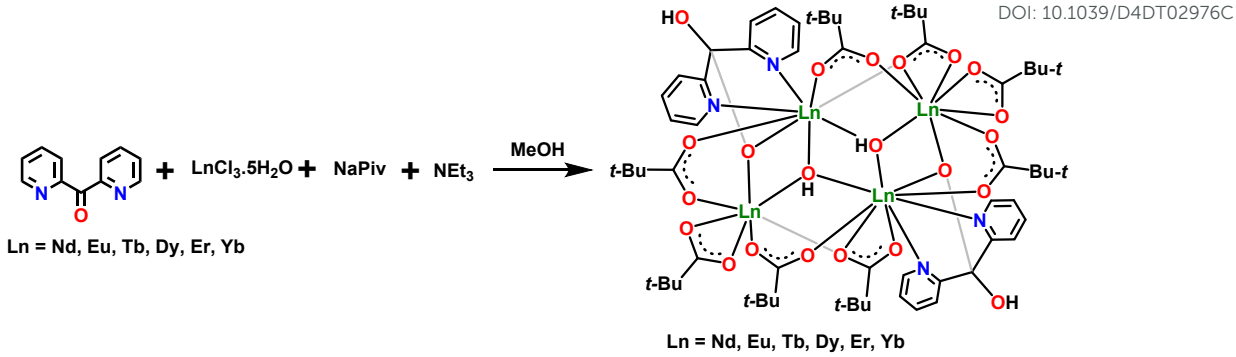

Scheme 1. Synthesis of tetranuclear Ln^{III}_4 complexes **1-6**.

Molecular structures of 1–6

The molecular structures of all the complexes **1-6** were determined by single crystal X-ray diffraction. The crystallographic parameters of **1–6** are given in Tables S**1-S2**. X-ray crystallographic analysis has revealed that complexes **1-6** are isomorphic. All the isostructural complexes crystallize in the monoclinic system with *C*2/*c* (*Z* = 4) space group. The asymmetric unit of all the compounds contains half of the total molecule, $[Ln_2(\mu_3\text{-}OH)\{py_2C(OH)O\}(O_2CCMe_3)_4]$, and a representative example is shown in **Chart 2 and Figure 1**. In view of the structural similarity, only compound **4** will be described in the main manuscript, and the remaining structural details parameters are given in the Supporting Information (Figures **S1-S5**).

The molecular structure of **4** is given in **Scheme 1 and Figure 2**. The tetranuclear homometallic lanthanide complex is built through the multiple coordination action of two $[\{py_2C(OH)O\}]^-$, two μ_3-OH, and eight bridging pivalate ligands. The coordination modes observed for all the ligands are displayed in **Chart 3**. Each $[\{py_2C(OH)O\}]^-$ ligand holds two Dy(III) ions via a chelating and bridging coordination mode of mono-anionic gemdiol (η^1: η^2: η^1: μ_2) and the Dy-O bond distances are Dy(1)-O(1), 2.289(2) Å and Dy(2)-O(1), 2.275(2) Å (**Figure 2** and **Scheme 1**). The two nitrogen centers of $[\{py_2C(OH)O\}]^-$ ligand exclusively bind in a η^1: η^1 fashion to the Dy1 center. The Dy-N bond distances are Dy(1)-N(2), 2.537(2) Å and Dy(1)-

View Article Online
DOI: 10.1039/D4DT02976C

N(1), 2.584(3) Å and the corresponding bite angle <N(2)-Dy(1)-N(1) is 69.58(8)º. In addition, there are three types of binding coordination modes of pivalate ligands (**Chart 3**), two of them act in a chelate fashion while the remaining six are bridged between the two Dy(III) centers. Finally, the four Dy(III) ions are held together by μ_3-OH bridging ligands, and the corresponding Dy-O bond distances are Dy1-O3, 2.335(2) Å; Dy1*-O3, 2.413(2) Å, and Dy2-O31, 2.360(2) Å. The core structure consists of two incomplete cubic sub-units that can be designated as *O-capped* clusters (two Dy_3O_4 units) (**Figure 3**). Similar types of structural motifs have been observed in main-group, 3d, 3d/4f, and 4f chemistry.[21]

There are two types of Dy(III) centers present and both are octa-coordinated. The coordination environment of Dy(1) and Dy(1)* centers are O_6N_2 while the Dy(2) and Dy(2) * centers are O_8. Systematic Shape analysis of compound **4**, using SHAPE 2.1,[22] indicates that the Dy(1) possesses a distorted elongated trigonal bipyramid geometry (**Figure 4a**), while the Dy(2) centers hold a distorted Johnson elongated triangular bipyramid geometry (**Figure 4b**) respectively. The full shape analysis results can be found in the Supporting Information (**Tables S3**). A mean plane analysis of core **4** reveals that all four Dy(III) centers are co-planar and present in the same plane (**Figure 5**). Interestingly, out of two bridging μ_3-OH ligands, one lies above the plane while the other one lies below the plane and caps the three Dy(III) centers (**Figure 5**). The distance between Dy(1) and Dy(2) is 3.696(7) Å, and for Dy(2) and Dy(1)* is 3.838(9) Å respectively. Interestingly, all the compounds possess a non-coordinated free OH group from the *gem* diol form of the $(py)_2CO$ ligand that generates strong intramolecular hydrogen bonding with the chelated coordinated pivalate ligand to the Dy2 center (H-bond between O2-H2⋯O8 atoms) (**Figure 6 and Table S4**). The H-bond distances are O2-H2⋯O8 1.981(7) for **1**; 1.933(4) Å for **2**; 1.925(5) Å for **3**; 1.917(3) Å for **4**; 1.894(5) Å for **5** and 1.923(3) Å for **6 (Figure S6)**, respectively. The H-bond distances decrease from

compound **1** to **6** due to lanthanide contraction **(Figure S6 and Table S4)**. As the size of the lanthanide ions decreases, the corresponding H-bond values diminish.

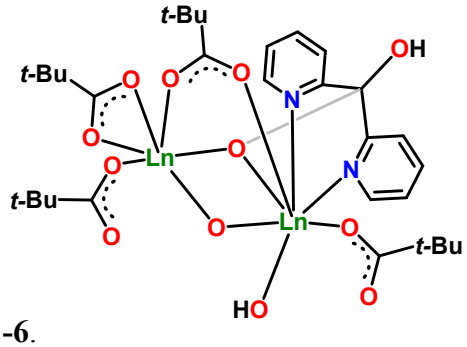

Chart 2. Asymmetric unit of **1-6**.

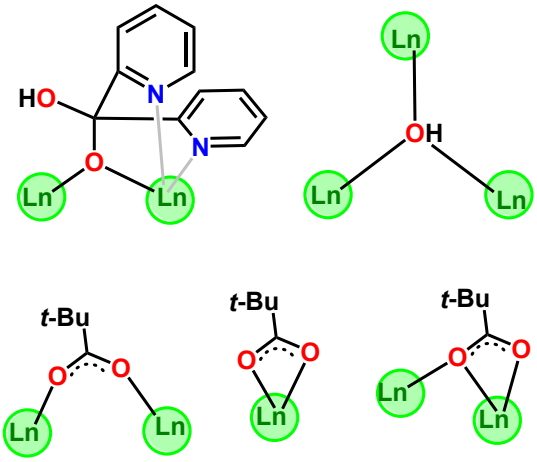

Chart 3. The coordination modes of all of the ligands were observed in the present study.

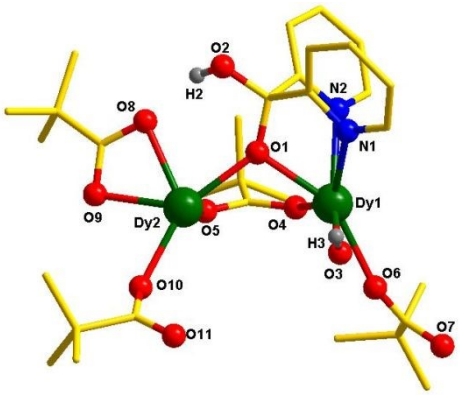

Figure 1. The asymmetric unit of **4**. All hydrogen atoms have been omitted for clarity.

View Article Online
DOI: 10.1039/D4DT02976C

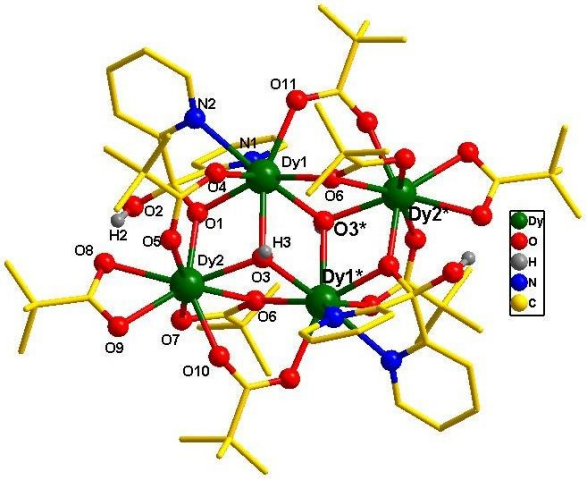

Figure 2. Molecular structure of **4**. All hydrogen atoms have been omitted for clarity. Symmetry codes: Dy2* (1-x, 1-y, 1-z), O3* (1-x, 1-y, 1-z).

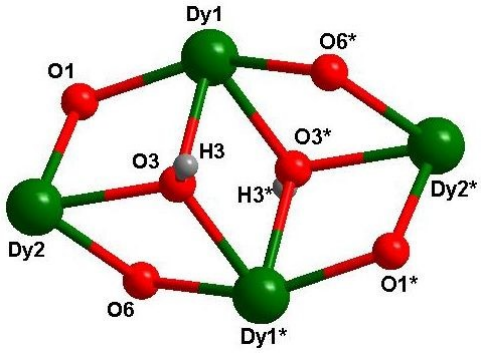

Figure 3. The *O-capped* core structure of **4**. Symmetry codes: Dy2* (1-x, 1-y, 1-z), O3* (1-x, 1-y, 1-z).

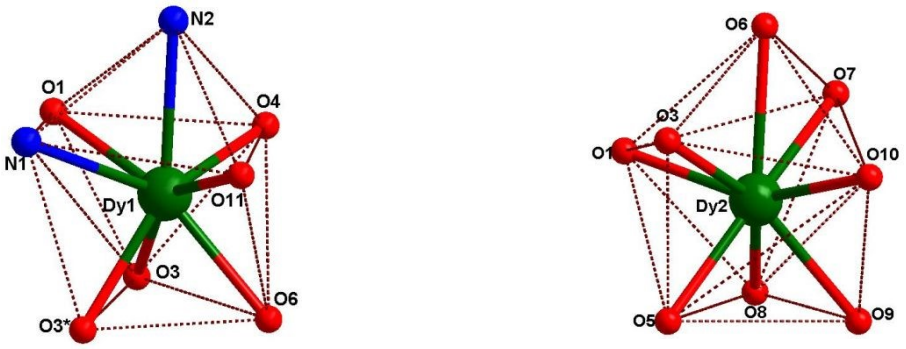

(a) **(b)**

Figure 4. The coordination geometry around the dysprosium centers is (a) distorted Elongated trigonal bipyramid and (b) distorted Johnson elongated triangular bipyramid of **4**.

View Article Online
DOI: 10.1039/D4DT02976C

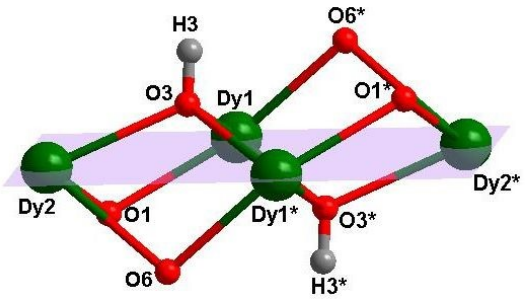

Figure 5. The mean plane through all four Dy(III) ions in compound **4**.

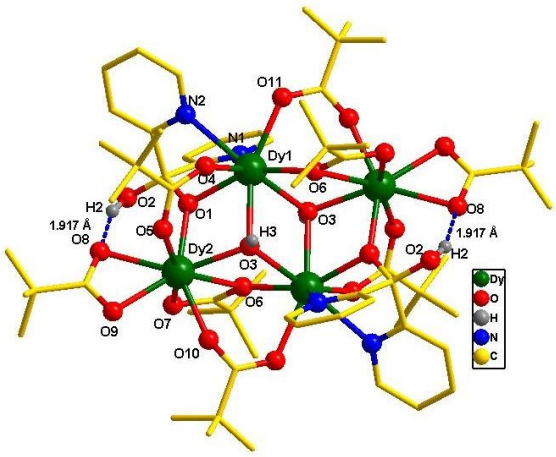

Figure 6. Intramolecular hydrogen bonding of **4**.

Luminescence properties

The UV-vis spectrum of compound **4** was recorded in a methanol solution (**Figure S7**). The absorption peak at 270 nm is assigned to the π–π* transitions of the $(py)_2CO$ ligand.

The photoluminescence studies of **1**-**5** were conducted at room temperature in the solid state. When excited at 270 nm in the solid state at room temperature, all the complexes show a bright intense emission peak at ~306 nm (**Figure 7a**) that originates from ligand-centred transitions. Indeed, for **3**, an additional intense sharp band at 490 nm is observed, due to the *f-f* microstate transition $^5D_4 \rightarrow {}^7F_6$ of the Tb^{3+} ion (**Figure 7b**).[23]

View Article Online
DOI: 10.1039/D4DT02976C

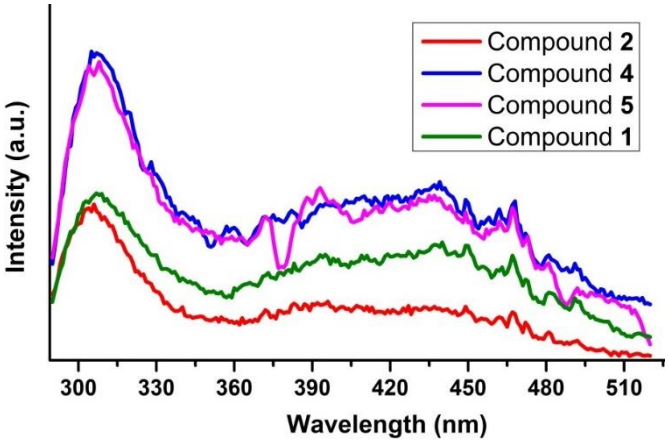

(a)

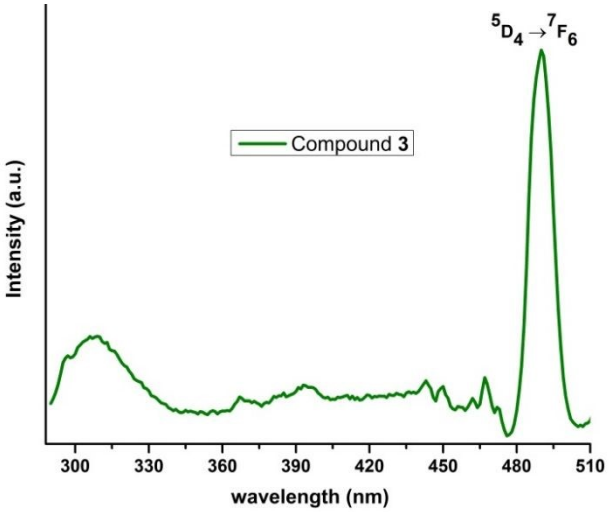

(b)

Figure 7. The luminescence emission spectra of complexes (a) for **1**-**2** and **4**-**5** (b) for **3**, in the solid state at room temperature upon excitation at 270 nm.

Exciting complex **1** at 380 nm, in the solid state at room temperature, causes emissions at 517, 624, and 724 nm. The peaks at 517, 624, and 724 nm are ascribed to the $^4I_{9/2} \rightarrow {}^4G_{7/2}$, $^4I_{9/2} \rightarrow {}^2H_{11/2}$ and $^4I_{9/2} \rightarrow {}^4F_{7/2} + {}^4S_{3/2}$ transitions respectively (**Figure S8**).[24]

For **2,** emission peaks at 394, 562, 592, 613, and 630 nm are observed, when excited at 330 nm. As mentioned above, the intense emission peak at 394 nm stems from the O-Eu transition and reveals that the $(py)_2CO$ ligand fluorescence is more dominating than that of the Eu^{3+} ion.[25] Other emission peaks are assigned to the $^5D_0 \rightarrow {}^7F_0$, $^5D_0 \rightarrow {}^7F_1$, $^5D_0 \rightarrow {}^7F_2$, and $^5D_0 \rightarrow {}^7F_3$ transitions (**Figure S9**).[26] The very weak band is responsible for the formally Laporte forbidden

$^5D_0 \rightarrow {}^7F_0$ transition. On the other hand, intensity enhanced for the magnetic dipole $^5D_0 \rightarrow {}^7F_1$ and forced electric dipole $^5D_0 \rightarrow {}^7F_2$ transitions which suggested a reduced symmetry of the europium coordination environment, both are eight-fold coordinated and consistent with the crystallography and shape analysis studies.[26]

Complex **3**, excited at 360 nm shows a blue emission peak at 493 nm caused by the $^5D_4 \rightarrow {}^7F_6$ transition. An intense green emission at 548 nm, yellow emission at 586, and red emission at 622 nm are ascribed for $^5D_4 \rightarrow {}^7F_5$, $^5D_4 \rightarrow {}^7F_4$, and $^5D_4 \rightarrow {}^7F_3$ transitions respectively (**Figure 8**).[23] The assigned peaks are well in agreement with luminescent Tb^{3+}complexes reported previously.[23]

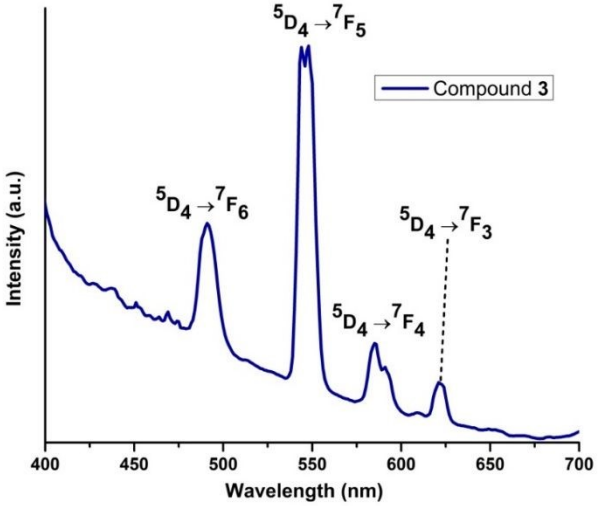

Figure 8. Room-temperature solid-state emission spectrum for complex **3** excited at 360 nm.

Exciting complex **4** at 310 nm in the solid state at room temperature, leads to luminescence peaks at 560, and 591 nm. The peaks at 560, and 591 nm are assigned to the transitions of $^4F_{9/2} \rightarrow {}^6H_{13/2}$ and $^4F_{9/2} \rightarrow {}^6H_{11/2}$, respectively for Dy^{3+} center emission (**Figure S10**).[23,27]

It is important to compare the existing reported lanthanide complexes based on the neutral $(py)_2CO$ or deprotonated form of the gem-diol $\{(py)_2(OH)CO\}^-$ or $\{(py)_2CO_2\}^-$] or hemiacetal form [$\{(py)_2(OR)CO\}^-$; R= Me, Et] with the current work. The literature survey revealed that few lanthanide complexes are known based on $(py)_2CO$ and its different forms of the ligands

View Article Online
DOI: 10.1039/D4DT02976C

(*vide supra*). It has been seen that all reported lanthanide complexes are either mono- or di-nuclear derivatives (**see Table S5**) and assembled by the formation of the monoanionic *gem*-diol [{$(py)_2(OH)CO$}$^-$ or hemiacetal [{$(py)_2(OR)CO$}$^-$; R= Me, Et] ligands. To the best of my knowledge, there are no such lanthanide complexes reported utilized by neutral $(py)_2CO$ or di-deprotonated form of [{$(py)_2CO_2$}$^-$ ligands. The first luminescent, mono and dinuclear Er(III) complexes, $[Er(NCS)_3\{(py)_2C(OR)(OH)\}_3]$, and $[Er_2(NCS)_3\{(py)_2C(OMe)O\}_3(MeOH)]$ reported in 2006.[28] These complexes are formed due to the hemiacetal formation {$(py)_2(OEt)COH$} and {$(py)_2(OMe)COH$} of the $(py)_2CO$ ligand. The analogous dinuclear derivatives, $[Ln_2(NO_3)_3\{(py)_2C(OMe)O\}_2\{(py)_2C(OH)O\}]$ [Ln = Tb and Er] have been synthesized by the reaction of $(py)_2CO$ with $Er(NO_3)_3{\cdot}6H_2O$ salt. The dinuclear complexes formed through the multiple bridging coordination action of the *gem*-diol {$(py)_2(OH)CO$}$^-$ and hemiacetal form [{$(py)_2(OMe)CO$}$^-$ of the $(py)_2CO$ ligand.[29] There are two types of Er(III) centers were observed. One Er(III) center is nine-coordinated with a distorted tricapped trigonal-prismatic geometry, and the other is eight-coordinated with a distorted dodecahedral geometry. The solid-state at room temperature luminescent study of the analogous dinuclear Eu^{III} and Tb^{III} complexes showed red and green emissions.[29] Similar type acetal formation has been reported by single crystal x-ray crystallography for $[Ln(NCS)_3\{(py)_2C(OEt)(OH)\}_3]$ [Pr(III), Sm(III) and Gd(III)] complexes.[30] There is one tetrahedral shape tetranuclear complex, $[Dy_4(NO_3)(HL)_4\{(py)_2C(OH)O\}_2]{\cdot}(OH){\cdot}6CH_3CN{\cdot}0.5H_2O)$ reported utilized the Schiff base 2-((2-hydroxybenzylidene)amino) propane-1,3-diol ligand (H_3L) and mono-deprotonated form of gem-diol, [$(py)_2(OH)CO$]$^-$ of the $(py)_2CO$ ligand.[31] Here {$(py)_2(OH)CO$}$^-$ acts as an auxiliary coordinating ligand. This complex showed slow magnetic relaxation at low temperatures. The nonnuclear derivative $[Dy_9(\mu_3\text{-}OH)_8(\mu_4\text{-}OH)_2(N_3)_8\{(py)_2C(OCH_3)O\}_8]{\cdot}(OH){\cdot}(4H_2O)$ has been synthesized by the reaction of $(py)_2CO$, NaN_3 and $Dy(NO_3)_3{\cdot}5H_2O$. This complex is formed by the hemiacetal {$(py)_2(OMe)CO$}$^-$ and showed slow relaxation of magnetization.[32]

View Article Online
DOI: 10.1039/D4DT02976C

Theoretical Studies and Magnetic Properties

Here, we have carried out ab initio calculations to shed light on the magnetic anisotropy and magnetic relaxation pathways in **1-6** complexes. All these calculations were carried out using the OpenMOLCAS code.[33] Complete active space self-consistent field (CASSCF) calculations were carried out using an active space of CAS(*n*,7) (where *n* = 3 (Nd (III)), 6 (Eu(III)), 9 (Dy(III)), 8 (Tb(III)), 11 (Er(III)) and 13 (Yb(III)) ions) to compute the spin-free and spin-orbit states. Next, we mixed these spin-free states using the restricted active space state interaction-spin orbit (RASSI-SO) module and computed the spin-orbit states. Subsequently, we used the SINGLE_ANISO module to extract the relevant spin-Hamiltonian parameters for **1-6** complexes. This methodology has been used widely to compute the electronic and magnetic properties of mononuclear and polynuclear lanthanide complexes.[34-35] To compute the single-ion anisotropy in the complexes, we substituted three Ln(III) ions with a diamagnetic Lu(III) ion and performed CASSCF calculations on the paramagnetic Ln(III) ions. Complexes **1-6** are tetranuclear complexes, where two dimeric $[Ln_2(\mu_3\text{-OH})\{py_2C(OH)O\}(O_2CCMe_3)_4]$ [where Ln = Nd (**1**), Eu (**2**), Tb (**3**), Dy (**4**), Er (**5**) and Yb (**6**)] units are bridged through the μ_3-OH and $\{py_2C(OH)O\}^-$ ligands. In complexes **1-6**, there are two types of eight-coordinated Ln(III) centres with [$\{LnO_8\}$ and $\{LnO_6N_2\}$] possessing distorted elongated trigonal bipyramid and distorted Johnson elongated triangular bipyramid geometry, respectively. Here, we named individual centres Ln@X (Ln = Nd, Eu, Tb, Dy, Er, and Yb, X = 1-4 (centre position) in complexes **1-6**, respectively). Due to the presence of the inversion symmetry, Ln@1/Ln@3 possess [$\{LnO_8\}$ core, while the Ln@2/Ln@4 $\{LnO_6N_2\}$ core is in complexes **1-6**.

In case of complex **1**, the ground state of Nd(III) possesses a $^4I_{9/2}$ term, and here, using an active space of CAS(3, 7), we computed all 35 quartets. For the Nd@1/3 and Nd@2/4 centres, the energies of five low-lying Kramers doublets (KDs) span over an energy range of ~363 and

View Article Online
DOI: 10.1039/D5DT02976C

~357 cm^{-1}, with the first excited state at ~ 82 and ~ 72 cm^{-1}, respectively. The ground state *g*-tensors for Nd@1 and Nd@2 centres are g_{xx} = 0.955, g_{yy} = 1.818, g_{zz} = 3.854 and g_{xx} = 3.422, g_{yy} = 2.457, g_{zz} = 0.646, respectively (see Table S12). The wave function analysis shows a m_J = |7/2⟩ ground state for Nd@1 and a m_J = |3/2⟩ ground state for Nd@2, along with a strong mixing from other excited states. The *g*-tensors for the first excited state are g_{xx} = 0.553, g_{yy} = 1.165, g_{zz} = 2.772 for Nd@1 and g_{xx} = 0.645, g_{yy} = 1.245, g_{zz} = 3.316 for Nd@2. Moreover, we have observed a large k_{QTM} of 0.46 μ_B for Nd@1 and 0.98 μ_B for Nd@2 within the ground state KDs, which sets the U_{cal} to be ~ 82 and ~ 72 cm^{-1} for Nd@1 and Nd@2, respectively. The Kramers' ion with substantial k_{QTM} at ground state KDs speeds up the magnetic relaxation, and diminishes the SMM behaviour in **1**. Next, we computed the crystal field (CF) using the following equation $H_{CF} = \sum_{k=2,4,6} \sum_{q=-k}^{q=+k} B_k^q \hat{O}_k^q$, where, $\hat{O}_k^q$ represents the extended Stevens operator and B_k^q is the crystal field parameter. The crystal field parameters (B_k^q) for all four individual Nd(III) centers of **1** are reported in Table S13. In all four cases, we observed computed axial B_k^q (k = 0, q = 0) and nonaxial B_k^q (k ≠ 0, q = 2, 4) parameters are competing with each other, which indicates that the crystal field generated by ligands is not completely axial in nature. This is also reflected in the computed transverse component of *g*-values, which are very large, leading to the large k_{QTM} value. Our spin-Hamiltonian (SH) analysis indicates a very fast QTM within the ground state, which diminishes any slow relaxation at the single-ion level.

Complex **2** possesses Eu(III) ions with [Xe] $4f^6$ electronic configuration, and the spin-orbit coupling stabilizes an isotropic $^7F_0$ term as the ground state. Using an active space of CAS(6,7), we computed 7 septets and 140 quintets, and the computed spin-free septet states span over an energy window of ~ 636.0 (642.9) cm^{-1}, for Eu@1/3 (Eu@2/4), respectively, while the quintet states span over an energy range of 90620.2 (90709.3) cm^{-1} for Eu@1/3 (Eu@2/4), respectively. RASSI-SO computed the first excited KD emerging from $^7F_1$ term located at

View Article Online
DOI: 10.1039/D4DT02976C

274.7 cm^{-1} and 258.2 cm^{-1} for the Eu@1/3 and Eu@2/4, respectively, with a $m_J = 0$ as ground state for Eu(III) Table S14. The computed χT behaviour shows a weak temperature-independent paramagnetism behaviour (see Figure 11).

In complex **4**, the eight low-lying Kramers doublets (KDs) derived from the $^6H_{15/2}$ state span over an energy range of 481.3 and 383.1 cm^{-1}, with the first excited KD located at ~ 133 and 36 cm^{-1} for the Dy@1/3 and Dy@2/4, respectively. For Dy@1/3 the centres, the computed *g*-values are $g_{xx} = 0.087$, $g_{yy} = 0.201$, $g_{zz} = 19.477$ whereas, for Dy@2/4, *g*-values are $g_{xx} = 0.090$, $g_{yy} = 0.474$, $g_{zz} = 17.333$. While both the centres exhibit axial anisotropy, the Dy@2/4 centres lack the Ising-type feature (g_{zz} ~ 20), as observed in Dy@1/3 (see Table S15). Wavefunction decomposition analysis shows stabilization of pure m_J $|\pm 15/2\rangle$ for Dy@1/3, while a mixed ground state composition of 64% $|\pm 15/2\rangle$ and 28% $|\pm 11/2\rangle$ was observed for the Dy@2/4 centres. The first excited KD, mainly $|\pm 11/2\rangle$, located at ~ 36 cm^{-1}, strongly mixes with the ground state KD, resulting in the mixed ground state configuration and decreased axiality in the ground state *g*-values for the Dy@2/4. The computed central magnetic axis (g_{zz}) for the Dy@1/3 is aligned towards the O atom of the ligand (~ 5.2°) and perpendicular to the plane formed for the five O donor atoms (see Figure 9a, 10a). On the other hand, the ground state g_{zz} axis is aligned towards the μ_3-OH ligand, possessing the largest negative Loprop charges (~ 23°) (see Figure 9b). Due to the non-superposition of the orientation of the ground and first excited KDs, it suggests that the magnetic relaxation is likely to occur via the first excited KD, resulting in the U_{cal} value of ~133 and 36 cm^{-1} for the Dy@1/3 and Dy@2/4 centres, respectively. (see Figure S13). In addition, due to the sizable transverse magnetic moment (7.2 × 10^{-2} μ_B for Dy@1/3 and 9.4 × 10^{-2} μ_B for Dy@2/4) within the ground state KDs, the quantum tunnelling of magnetization (QTM) is likely to be a competing mechanism for magnetic relaxation. This discrepancy in the *g*-values and computed U_{cal} values for both centres is attributed to the differences in the local structural environment, which is reflected in the

computed crystal field parameters. For both the centers, we observed that the non-axial B_k^q terms ($q \neq 0$ and $k = 2, 4$) are dominant and compete with the axial parameters ($q = 0$ and $k = 2, 4$) terms (see Table S16), which clearly reflects that the ligand field around both the Ln(III) centres is not completely axial anisotropic in nature. Secondly, the computed axial crystal field parameters are -1.58 for Dy@1/3 and -7.06×10^{-01} for Dy@2/4 centres, a ~10x times weaker for Dy@2/4 centres, highlighting why the first excited KD is much lower in energy for the Dy@2/4 centre.

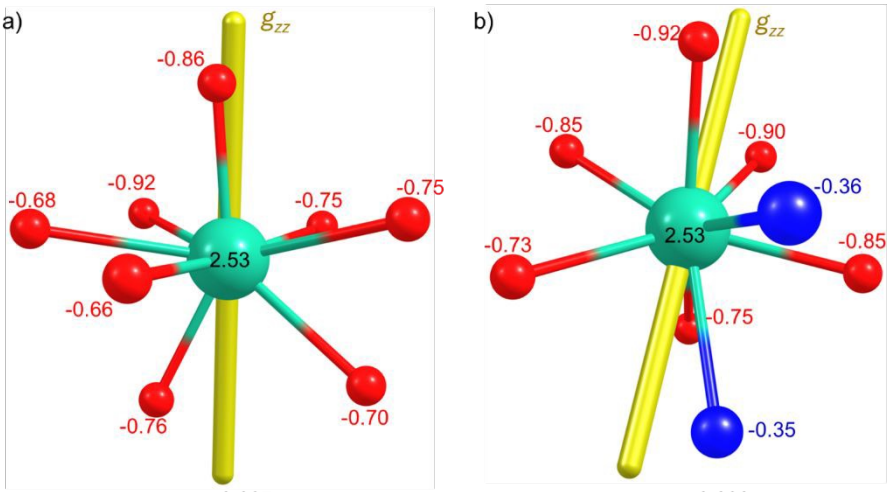

Figure 9. CASSCF computed LoProp charges on the Dy@1 (a) Dy@2 (b) first coordination sphere ligated atoms, along with the orientation of the main magnetic axis g_{zz} in complex **4**.

For complex **3**, the low-lying pseudo-doublets derived from the ground $^7F_6$ multiplets span ~499 (352) cm^{-1} with the first excited state at 118.7 (63.9) cm^{-1} for Tb@1/3 (Tb@2/4) centres. Due to the similarity in the local structural parameters, the splitting pattern for Tb(III) centres are two distinct Dy centers in the **4**. Wavefunction decomposition analysis predicts a pure 98% $|\pm6\rangle$ for centres Tb@1/3 and a mixed m_J state 84% $|\pm6\rangle$ + 12% $|\pm4\rangle$ as the ground state Tb@2/4. The computed ground state *g*-values are highly axial, with g_{zz} ~ 17.797 (17.049) and with substantial ground state tunnel splitting of 0.2 (0.7) cm^{-1} for Tb@1/3(Tb@2/4) centres

View Article Online
DOI: 10.1039/D4DT02976C

(see Table S17). CASSCF computed that the main magnetic axes of the ground state are oriented towards the -O atom (30 degrees) of the ligand for Tb@1/3 and N (33°) of the ligand for Tb@2/4 (see Figure 9, 10b), in a similar fashion to what was observed for Dy(III) centres in complex **4**. The computed U_{cal} values are ~ 118.7 (63.9) cm^{-1} for Tb@1/3(Tb@2/4) with large ground state tunnel splitting. Due to large tunnel splitting in non-Kramer ions, the QTM is likely to be the dominant mechanism of magnetic relaxation in complex **3**. The computed CF parameters show significant non-axial terms, indicating that the local ligand field around the Tb@1/3 and Tb@2/4 centres is non-axial, resulting in the giant QTM within the ground state pseudo-KDs (see Table S18).

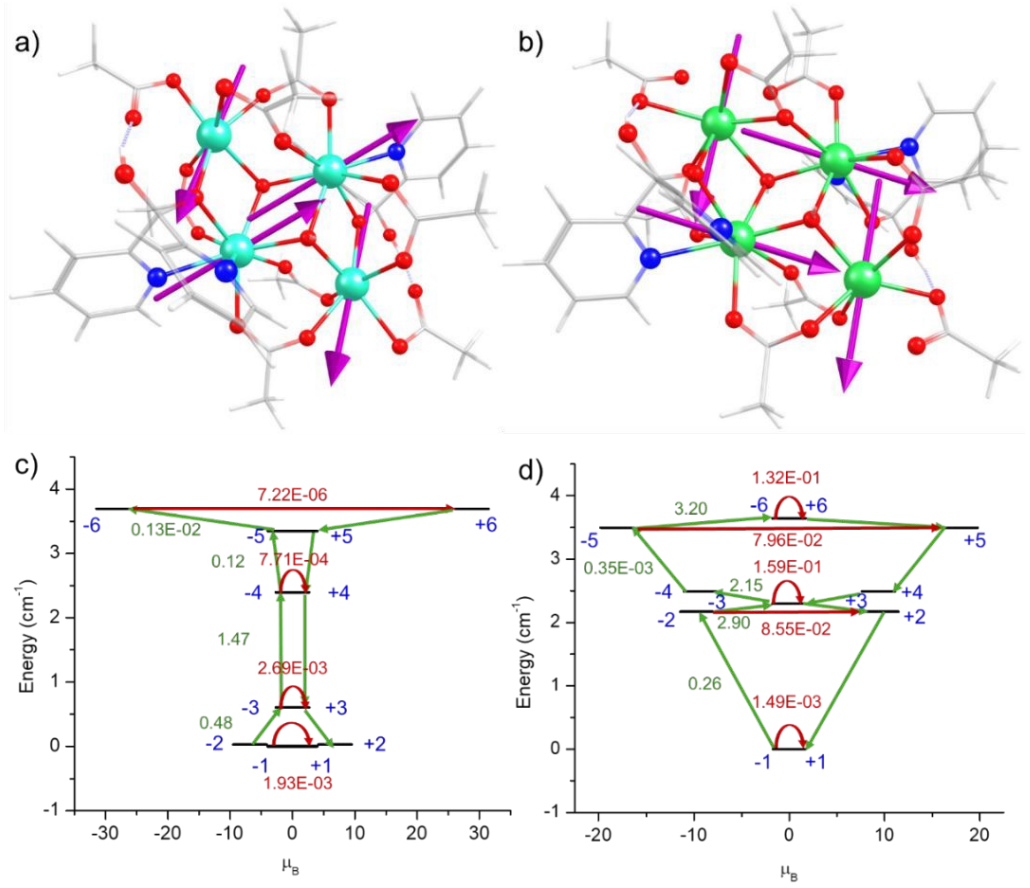

Figure 10. SINGLE_ANISO computed orientation of the ground state main magnetic axis (g_{zz}) of the individual centres in a) complex **4**; b) complex **3,** and POLY_ANISO computed *ab initio*

View Article Online
DOI: 10.1039/D4DT02976C

blockade barrier for a) complex **4**; b) complex **3**. [Color code: teal (Dy), green (Tb), red (O), blue (N), grey (C), white (H).

In complex **5**, we computed all 35 quartets using an active space of CAS (11,7). The calculated spectrum of the spin-free quartet states spanned over an energy window of ~ 46977.7 (46961.0) cm^{-1} for Er@1/3 (Er@2/4), respectively. RASSI-SO computed energy spectrum of eight low-lying Kramers doublets (KDs) derived from the $^4I_{15/2}$ state spans over an energy range of 304 and 318 cm^{-1}, with the first excited KD located at ~ 29 and 22 cm^{-1} for the Er@1/3 and Er@2/4, respectively. For Er@1/3 the centres, the computed *g*-values are g_{xx} = 2.348, g_{yy} = 2.782, g_{zz} = 12.600 whereas, for Er@2/4, *g*-values are g_{xx} = 0.951, g_{yy} = 2.035, g_{zz} = 14.646 (see Table S23) (Table S23). While both the centres exhibit axial anisotropy, they lack the Ising-type feature (g_{zz} ~ 20), as they possess a significant transverse component. Wavefunction decomposition analysis shows stabilisation of pure m_J |±15/2⟩ as the ground state for both the Er(III) centres. The first excited KD has the *g*-values of g_{xx} = 7.267, g_{yy} = 5.607, g_{zz} = 2.324, and g_{xx} = 0.183, g_{yy} = 2.639, g_{zz} = 12.654 for Er@1 and Er@2, respectively. Similar to complex **1**, a large k_{QTM} (0.86 μ_B for Er@1 and 0.50 μ_B for Er@2) is observed for Er(III) centres, which suggests dominance of the QTM in the ground state. This is further supported by the computed CF parameters (see Table S24), where non-axial terms are significantly larger than the axial terms. In complex **6**, the ground state of Yb(III) possesses a $^2F_{7/2}$ term, and here, using an active space of CAS (13,7), we computed all 7 septets. The four Kramers doublets generated from the $^2F_{7/2}$ state span up to 376.9 cm^{-1} and 460.7 cm^{-1} for Yb@1/3 and Yb@2/4, respectively. For Yb@1/3 the centres, the computed *g*-values are g_{xx} = 1.434, g_{yy} = 1.908, g_{zz} = 6.308, whereas, for Yb@2/4, *g*-values are g_{xx} = 0.615, g_{yy} = 1.122, g_{zz} = 7.323 with large k_{QTM} of 0.56 μ_B for Yb@1 and 0.29 μ_B for Yb@2 for the ground state KD (see Table S25). The strong transverse anisotropy results in the large k_{QTM} value within the ground state connecting doublet, which indicates the presence of strong ground-state QTM. The computed CF parameters show large

View Article Online
DOI: 10.1039/D4DT02976C

and sizable non-axial terms, which compete with the axial term, highlighting a mixed crystal field significantly enables the ground state QTM. (see Table S26).

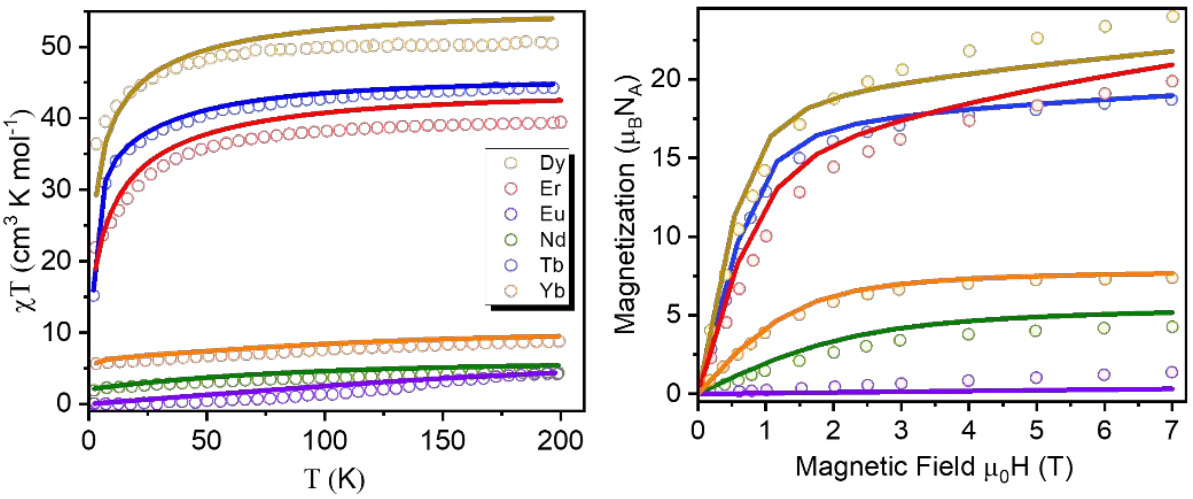

Figure 11. Thermal dependence of the molecular magnetic susceptibility for Ln_4 complexes (left). The simulated results are scaled up by 3% in order to make it compatible with experimental data. Magnetization (M) versus Magnetic Field (H) plot for all the complexes at 2K (right). The circles are the experimental values, while the line represents the POLY_ANISO simulated data.

Next, we extracted the magnetic exchange interaction between the Ln(III) centres in all he complexes by fitting the experimental static DC magnetic susceptibility and magnetization data (**Figure 11**). Here, we used the $\hat{H} = -\hat{J}(S_1 \cdot S_2)$ formalism using the POLY_ANISO code, where J is the magnetic exchange interaction that contains both the exchange ($\hat{J}_{ex}$) and dipolar coupling ($\hat{J}_{dipo}$), while S_1 and S_2 represent the projections of the pseudo-spin $S = ½$ of the ground state. The simulation nicely reproduces the experimental magnetic susceptibility data for complexes **1** - **6** (see Figure 11). All the complexes possess butterfly cores where two Ln(III) centres are in the body position while the other two Ln(III) centres are in the wing position, leading to three distinct magnetic exchange couplings (J_1–J_3) (see Figure S14 in ESI).

View Article Online
DOI: 10.1039/D5DT02976C

The best fit of experimental magnetic susceptibility (J_{total}) along with magnetic exchange values (J_{ex}) for complexes **1**–**6** are reported in Table 1.

Table 1. Exchange and dipolar interaction were obtained from the POLY_ANISO simulation from the best fit using the Lines model for **1-6** with zJ = -0.002

	1			**2**			**3**			**4**			**5**			**6**		
	J_1	J_2	J_3	J_1	J_2	J_3	J_1	J_2	J_3	J_1	J_2	J_3	J_1	J_2	J_3	J_1	J_2	J_3
J_{tot}	-0.06	-0.09	-0.04	-0.09	-0.07	-0.03	-0.10	-0.14	-0.06	-0.12	-0.14	-0.07	-0.15	-0.14	-0.09	-0.09	-0.08	-0.04
J_{ex}	-0.04	-0.07	-0.03	-0.08	-0.06	-0.02	-0.09	-0.12	-0.05	-0.07	-0.09	-0.06	-0.12	-0.11	-0.10	-0.07	-0.06	-0.03
J_{dipo}	-0.02	-0.02	-0.01	-0.01	-0.01	-0.01	-0.01	-0.02	-0.01	-0.05	-0.05	-0.01	-0.03	-0.03	0.01	-0.02	-0.02	-0.01

The best fit of experimental magnetic susceptibility yields a J_{total} of -0.10 (J_1), -0.14 (J_2), -0.06 (J_3) cm^{-1} for complex **4** while a J_{total} of -0.12 (J_1), -0.14 (J_2), -0.07 (J_3) cm^{-1} for complex **3** with a small intermolecular interaction z_J of −0.002 cm^{-1} for both the complexes (see Table S19 and S21).[34d] Additionally, we determined the contributions of J_{ex}/J_{dipo} to the J_{tot} values by turning off the dipolar interactions and the best-fit yields the J_{ex}/J_{dipo} value to be -0.09/-0.01, -0.12/-0.02, -0.05/-0.01 for complex **4** and −0.07/-0.05, -0.09/-0.05, -0.06/-0.01 cm^{-1} for complex **3**. It is evident from the fitting that both the exchange and dipolar interactions are antiferromagnetic in nature for both the complexes. Moreover, the exchange contributions (arises through bond and space) are much dominated by dipolar interactions. Next, we constructed the exchange spectrum of complexes **4** and **3**, where a non-Kramer-type exchange-coupled ground state is observed for both complexes (Figure 10c, d). In both complexes, the exchange-coupled ground state shows a g_{zz} value of ~ 2.6654 (**4**) and 0.0021

(**3**), resulting from the antiferromagnetic interaction between the Ln(III) centers (see Table S20 and S22). For both complexes **4** and **3**, we observed a sizable tunnel splitting of 1.9×10^{-3} cm^{-1} and 1.5×10^{-3} cm^{-1}, indicating that QTM is still a dominant mechanism for magnetic relaxation in the exchange-coupled systems, resulting in diminishing the SMM behaviour. Despite having a strong antiferromagnetic coupling between the Ln(III) centres, a distorted local geometry around the Ln(III) centre fails to isolate a large m_J as the ground state, which in turn diminishes the SMM behaviour for both complexes **3** and **4**.

In order to check experimentally whether these complexes exhibit slow spin-lattice relaxation, AC susceptibility has been measured at 2 K from 50 Hz to 10 kHz as shown in Figure S15 in the supplementary information. To suppress potential quantum tunnelling as relaxation process of magnetic reversal, the AC susceptibility has not only been measured at zero DC magnetic field, but also at various DC fields (up to about 2500 Oe for selected complexes). None of the complexes **1** (Nd), **3** (Tb), **4** (Dy), **5** (Er), and **6** (Yb) exhibits AC susceptibility data that would clearly indicate the existence of slow magnetic relaxation with a clear maximum of the imaginary χ'' signal within the available experimental parameter space. Only complex **3** (Tb) shows an increase of the χ'' signal close to the maximum frequency of 10 kHz that might indicate the presence of slow relaxation at even higher frequencies. For complex **2** (Eu) AC susceptibility could not be measured due to the weak magnetic signal at low temperature.

Conclusion

We have utilized di-2-pyridyl ketone ligand for first time to assemble the homometallic tetranuclear Ln^{III}_4 ensembles. The core structure of this family consists of two *O-capped* sub-units. The four Ln(III) ions are coplanar and lie in the same plane. Each complex contains two types of eight-coordinated lanthanide centers viz. the Ln1 center possesses a distorted elongated trigonal bipyramid geometry and the Ln2 center has a distorted Johnson elongated triangular bipyramid geometry. All the complexes show strong intramolecular hydrogen

View Article Online
DOI: 10.1039/D4DT02976C

bonding within the molecular integrity and the H-bond distances are decreases corresponding to their lanthanide contraction. Photoluminescence study of these complexes shows that the di-2-pyridyl ketone ligand sensitizes compound **3**, but for all other complexes, intense ligand center emission peaks are observed. For compound **3**, intense emission peaks at 493, 548, 586, and 622 nm are observed upon excitation at 360 nm in the solid state at room temperature. CASSCF calculations were performed on complexes **1-6** for magnetic anisotropy, magnetic relaxation pathways and crystal field (CF) splitting. We used the SINGLE_ANISO module to extract the relevant spin-Hamiltonian parameters for all the complexes. The Kramers' ion with substantial k_{QTM} at ground state KDs speeds up the magnetic relaxation, and diminishes the SMM behaviour in **1**. We computed the crystal field and observed that the axial parameters are competing each other which indicates that the crystal field generated by ligands is not completely axial in nature. Complexes **3** and **4** show that the distorted geometry around the Ln(III) centres fails to stabilize the largest m_J as the ground state, which in turn diminishes the SMM behaviour despite having sizable antiferromagnetic interaction between the Ln(III) centres. For 4, due to the non-superposition of the orientation of the ground and first excited KDs, it suggests that the magnetic relaxation is likely to occur via the first excited KD. We have calculated magnetic exchange interactions indicates three distinct magnetic couplings (J_1–J_3). AC susceptibility measurements of the complexes at 2 K did not exhibit any local maximum of the imaginary χ'' component that would have been characteristic for the realization of slow spin-lattice relaxation, neither at zero DC field nor at various DC fields. But complex **3** (Tb) shows an increase of the χ'' signal close to the maximum frequency of 10 kHz that might indicate the presence of slow relaxation at even higher frequencies. We are currently exploring the di-2-pyridyl ketone ligand-based lanthanide complexes by changing the reaction conditions which afforded different coordination numbers and geometry containing lanthanide clusters. These manuscripts are under preparation.

View Article Online
DOI: 10.1039/D4DT02976C

Acknowledgments

We thank the Department of Science Engineering Research Board (SERB), India, for the Ramanujan fellowship (**SERB/F/10742/202-2022**)) for financial support. JG is thankful to the Department of Chemistry, Jadavpur University, University of Delhi, and the Institution of Eminence (IoE) for the FRP research grant (**Ref. No./IoE/2023-24/12/FRP**). S. K. S. acknowledges the Science and Engineering Board (SERB) for the Core Research Grant (CRG/2023/002936) and IIT Hyderabad for generous funding. I. T. thanks UGC for the NFOBC fellowship.

Supporting Information Available: Figures and tabulated bond angles/lengths for crystal structures of compounds **1-6**. Full results of the SHAPE analysis for the Ln(III) centers in **1-6**. Figure S12 for IR spectrum of complexes **1-6**. Figures S15 are *Ac* susceptibility measurements for compounds **1-6**. The CIFs have been deposited with CCDC No. **2379210-2379215** for complexes **1-6**.

References

1. (a) D. N. Woodruff, R. E. P. Winpenny and R. A. Layfield, Lanthanide single-molecule magnets, *Chem. Rev*., 2013, **113**, 5110-5148. DOI: 10.1021/cr400018q; (b) J. Goura and V. Chandrasekhar, Molecular Metal Phosphonates, *Chem. Rev*., 2015, 115, 6854-6965. DOI: 10.1021/acs.chemrev.5b00107; (c) S.-R. Li, W.-D. Liu, L.-S. Long, L.-S. Zheng and X.-J. Kong, Recent advances in polyoxometalate-based lanthanide–oxo clusters, *Polyoxometalates*, 2023, **2**, 9140022. DOI: 10.26599/POM.2023.9140022.

2. (a) T. C. Stamatatos, C. G. Efthymiou, C. C. Stoumpos and S. P. Perlepes, Adventures in the Coordination Chemistry of Di-2-pyridyl Ketone and Related Ligands: From High-Spin Molecules and Single-Molecule Magnets to Coordination Polymers, and from Structural Aesthetics to an Exciting New Reactivity Chemistry of Coordinated Ligands, *Eur. J. Inorg. Chem*., 2009, 3361–3391. DOI: 10.1002/ejic.200900223; (b) G. S. Papaefstathiou and S. P.

Perlepes, Families of Polynuclear Manganese, Cobalt, Nickel and Copper Complexes Stabilized by Various Forms of Di-2-pyridyl Ketone, *Comments on Inorganic Chemistry: A Journal of Critical Discussion of the Current Literature*, 2002, **23**, 249-274, DOI: 10.1080/02603590213135.

3. H. Mori, K. Sakamoto, Y. Masudo, Y. Matsuoka, M. Matsubayashi, K. Sakai, Aerial Oxidation of Some 2-Pyridyl Ketone Hydrazones Catalyzed by Cu^{2+}. Physical Properties of Reaction Products, *Chem. Pharm. Bull*., 1993, **41**, 1944-1947. DOI: 10.1248/cpb.41.1944.

4. M. Shiddiq, D. Komijani, Y. Duan, A. Gaitaariño, E. Coronado and S. Hill, Enhancing coherence in molecular spin qubits via atomic clock transitions, *Nature*, 2016, **531**, 348–351. DOI: 10.1038/nature16984.

5. L. Bogani and W. Wernsdorfer, Molecular spintronics using single-molecule magnets, *Nature Mater*, 2008, **7**, 179–186. DOI: 10.1038/nmat2133

6. (a) (a) M. Mannini, F. Pineider, P. Sainctavit, C. Danieli, E. Otero, C. Sciancalepore, A. M. Talarico, M. A. Arrio, A. Cornia, D. Gatteschi and R. Sessoli, Magnetic memory of a single-molecule quantum magnet wired to a gold surface, *Nature Mater*, 2009, **8**, 194–197. DOI: 10.1038/nmat2374; (b) S. Thiele, F. Balestro, R. Ballou, S. Klyatskaya, M. Ruben and W. Wernsdorfer, Electrically driven nuclear spin resonance in single-molecule magnets, *Science*, 2014, **344**, 1135–1138. DOI: 10.1126/science.1249802.

7. Y. Z. Zheng, G. J. Zhou, Z. Zheng and R. E. P. Winpenny, Molecule-based magnetic coolers, *Chem. Soc. Rev*., 2014, **43**, 1462-1475. DOI: 10.1039/C3CS60337G.

8. Y. -J. Ma, J. -X. Hu, S. -D. Han, J. Pan, J. -H. Li and G. -M. Wang, Manipulating On/Off Single-Molecule Magnet Behavior in a Dy(III)-Based Photochromic Complex, *J. Am. Chem. Soc*., 2020, **142**, 2682–2689. DOI: 10.1021/jacs.9b13461.

9. J. D. Rinehart and J. R. Long, Exploiting single-ion anisotropy in the design of f-element single-molecule magnets, *Chem. Sci*., 2011, **2**, 2078-2085. DOI: 10.1039/C1SC00513H.

10. H. Schilder, and H. Lueken, Computerized magnetic studies on d, f, d–d, f–f, and d–s, f–s systems under varying ligand and magnetic fields, *J. Magn. Magn. Mater*. 2004, **281,** 17–26. DOI: 10.1016/j.jmmm.2004.03.041.

11. N. Ishikawa, Simultaneous Determination of Ligand-Field Parameters of Isostructural Lanthanide Complexes by Multidimensional Optimization, *J. Phys. Chem. A* 2003, **107**, 5831–5835. DOI: 10.1021/jp034433a

12. T. Han, Y.-S. Ding, J.-D. Leng, Z. Zheng and Y.-Z. Zheng, Polymeric Perturbation to the Magnetic Relaxations of the C_{2v}- Symmetric $[Er(Cp)_2(OBu)_2]^-$ Anion, *Inorg. Chem*., 2015, **54**, 4588–4590.

13. G. **Novitchi**, S. **Jiang**, S. **Shova**, F. **Rida**, I. **Hlavička**, M. **Orlita**, W. **Wernsdorfer**, R. **Hamze**, **C. Martins**, **N. Suaud**, **N. Guihéry**, A. -L. **Barra and** C. **Train**, From Positive to Negative Zero-Field Splitting in a Series of Strongly Magnetically Anisotropic Mononuclear Metal Complexes*, Inorg. Chem.*, 2017, **56**, 24, 14809–14822. **DOI: 10.1021/acs.inorgchem.7b01861**

14. (a) V. Vieru, S. Gómez-Coca, E. Ruiz and L. F. Chibotaru, Increasing the Magnetic Blocking Temperature of Single-Molecule-Magnets, *Angew. Chem. Int. Ed*., 2024, **136**, e202303146. DOI:10.1002/anie.202303146; (b) F.-S. Guo, B. M. Day, Y.-C. Chen, M.-L. Tong, A. Mansikkamäki and R. A. Layfield, Magnetic hysteresis up to 80 kelvin in a dysprosium metallocene single-molecule magnet, *Science*, 2018, **362**, 1400–1403. DOI: 10.1126/science.aav0652.

15. (a) T. Pugh, N. F. Chilton, and R. A. Layfield, A Low-Symmetry Dysprosium Metallocene Single-Molecule Magnet with a High Anisotropy Barrier, *Angew. Chem. Int. Ed.*, 2016, **55**, 11082–11085. DOI: 10.1002/anie.201604346; (b) J. C. Vanjak, B. O. Wilkins, V. Vieru, N. S. Bhuvanesh, J. H. Reibenspies, C. D. Martin, L. F. Chibotaru and M. Nippe, A High-Performance Single-Molecule Magnet Utilizing Dianionic Aminoborolide Ligands, *J. Am.*

Chem. Soc., 2022, **144**, 17743−17747. DOI: 10.1021/jacs.2c06698; (c) J. Tang, and P. Zhang, Lanthanide single molecule magnets, Springer Berlin Heidelberg, 2015.

16. (a) S. Mondal, D. Chauhan, T. Guizouarn, F. Pointillart, G. Rajaraman, A. Steiner and V. Baskar, Self-Assembled Lanthanide Phosphinate Square Grids (Ln = Er, Dy, and Tb): Dy_4 Shows SMM/SMT and Tb_4 SMT Behavior, *Inorg. Chem*., 2024, DOI:10.1021/acs.inorgchem.4c02567 (references therein); (b) P. Kumar, A. Swain, J. Acharya, Y. Li, V. Kumar, G. Rajaraman, E. Colacio and V. Chandrasekhar, Synthesis, Structure, and Zero-Field SMM Behavior of Homometallic Dy_2, Dy_4, and Dy_6 Complexes, *Inorg. Chem.*, 2022, **61**, 11600-11621. DOI: 10.1021/acs.inorgchem.2c01041; (c) J. Goura, J. P. S. Walsh, F. Tuna and V. Chandrasekhar, Tetranuclear Lanthanide(III) Complexes in a Seesaw Geometry: Synthesis, Structure, and Magnetism, *Inorg. Chem.*, 2014, **53**, 3385-3391. DOI: 10.1021/ic4027915.

17. B.S. Furniss, A. J. Hannaford, P.W. G. Smith and A.R. Tatchell, *Vogel's Textbook of Practical Organic Chemistry, 5th ed*.; Longman: London, 1989.

18. (a) *SMART & SAINT Software Reference manuals*, Version 6.45; Bruker Analytical X-ray Systems, Inc.: Madison, WI, 2003. (b) Sheldrick, G. M. SADABS, a software for empirical absorption correction, Ver. 2.05; University of Göttingen, Göttingen, Germany, 2002. (c) SHELXTL Reference Manual, Ver. 6.c1; Bruker Analytical X-ray Systems, Inc.: Madison, WI, 2000. (d) Sheldrick, G. M. SHELXTL, Ver. 6.12; Bruker AXS Inc.: Madison, WI, 2001. (e) Sheldrick, G. M. SHELXL97, Program for Crystal Structure Refinement; University of Göttingen, Göttingen, Germany, 1997. (f) Bradenburg, K. Diamond, Ver. 3.1eM; Crystal Impact GbR: Bonn, Germany, 2005.

19. (a) A. J. Tasiopoulos and S. P. Perlepes, Diol-type ligands as central 'players' in the chemistry of high-spin molecules and single-molecule magnets, *Dalton Trans*., 2008, 5537–5555. DOI: 10.1039/b805014g; (b) C. G. Efthymiou, C. P. Raptopoulou, A. N. Georgopoulou,

A. Escuer, C. Papatriantafyllopoulou and S. P. Perlepes, Initial employment of di-2-pyridyl ketone as a route to nickel(II)/lanthanide(III) clusters: triangular Ni_2Ln complexes, *Dalton Trans*., 2010, **39**, 8603–8605. DOI: 10.1039/c0dt00493f; (c) C. G. Efthymiou, T. C. Stamatatos, C. Papatriantafyllopoulou, A. J. Tasiopoulos, W. Wernsdorfer, S. P. Perlepes and G. Christou, Nickel/Lanthanide Single-Molecule Magnets: $\{Ni_3Ln\}$ "Stars" with a Ligand Derived from the Metal-Promoted Reduction of Di-2-pyridyl Ketone under Solvo thermal Conditions, *Inorg. Chem*., 2010, **49**, 9737–9739. DOI: 10.1021/ic101504c; (d) A. N. Georgopoulou, C. G. Efthymiou, C. Papatriantafyllopoulou, V. Psycharis, C. P. Raptopoulou, M. Manos, A. J. Tasiopoulos, A. Escuer and S. P. Perlepes, Triangular $Ni^{II}_2Ln^{III}$ and $Ni^{II}_2Y^{III}$ complexes derived from di-2-pyridyl ketone: Synthesis, structures and magnetic properties, *Polyhedron*, 2011, **30**, 2978–2986. DOI:10.1016/j.poly.2011.02.010; (e) M. Savva, K. Skordi, A. D. Fournet, A. E. Thuijs, G. Christou, S. P. Perlepes, C. Papatriantafyllopoulou, A. J. Tasiopoulos, Heterometallic $Mn^{III}_4Ln_2$ (Ln = Dy, Gd, Tb) Cross-Shaped Clusters and Their Homometallic $Mn^{III}_2Mn^{II}_2$ Analogues, *Inorg. Chem*., 2017, **56**, 5657-5668. DOI: 10.1021/acs.inorgchem.7b00191; (f) M. Savva, D. I. Alexandropoulos, M. Pissas, S. P. Perlepes, C. Papatriantafyllopoulou, Y. Sanakis and A. J. Tasiopoulos, Heterometallic clusters based on an uncommon asymmetric "V-shaped" $[Fe^{3+}(\mu\text{-}OR)Ln^{3+}(\mu OR)_2Fe^{3+}]^{6+}$ (Ln = Gd, Tb, Dy, Ho) structural core and the investigation of the slow relaxation of the magnetization behaviour of the $[Fe_2Dy]$ analogue, *Dalton Trans.*, 2023, **52**, 6997–7008. DOI: 10.1039/d2dt03938a.

20. R. Jagannathan and S. Soundararajan, Complexes of rare earth perchlorates with di-2-pyridyl ketone, *J. Inorg. & Nuclear Chem.*, 1980, **42**, 145-147. DOI: 10.1016/0022-1902(80)80066-2.

21. (a) R. O. Day, J. M. Holmes, V. Chandrasekhar and R. R. Holmes, A new structural form of tin in an oxygen-capped cluster, *J. Am. Chem. Soc.*, 1987, **109**, 940-941. DOI:

10.1021/ja00237a072; (b) D. Maniaki, E. Pilichos and S. P. Perlepes, Coordination Clusters of 3d-Metals That Behave as Single-Molecule Magnets (SMMs): Synthetic Routes and Strategies, *Front. Chem*., 2018, **6**, 461. DOI: 10.3389/fchem.2018.00461; (c) A. Das, F. J. Klinke, S. Demeshko, S. Meyer, S. Dechert and F. Meyer, Reversible Solvatomagnetic Effect in Novel Tetranuclear Cubane-Type Ni_4 Complexes and Magnetostructural Correlations for the [$Ni_4(\mu_3$-$O)_4$] Core, *Inorg. Chem.*, 2012, 51, 8141-8149. DOI : 10.1021/ic300535d ; (d) J. Wang, M. Feng, M. Nadeem Akhtar and M.-L.Tong, Recent advance in heterometallic nanomagnets based on TM_xLn_{4-x} cubane subunits, *Coord. Chem. Rev*., 2019, **387**, 129–153. DOI:10.1016/j.ccr.2019.02.008; (e) J. Goura, R. Guillaume, E. Rivière and V. Chandrasekhar, Hexanuclear, Heterometallic, Ni_3Ln_3 Complexes Possessing O-Capped Homo- and Heterometallic Structural Subunits: SMM Behavior of the Dysprosium Analogue, *Inorg. Chem*., 2014, **53**, 7815−7823. DOI: 10.1021/ic403090z; (f) J. Goura, A. Chakraborty, J. P. S. Walsh, F. Tuna and V. Chandrasekhar, Hexanuclear 3d–4f Neutral $Co^{II}_2Ln^{III}_4$ Clusters: Synthesis, Structure, and Magnetism, *Crystal Growth&Design*, 2015, **15**, 3157-3165. DOI: 10.1021/acs.cgd.5b00588; (g) B.-Q. Ma, D.-S. Zhang, S. Gao, T.-Z. Jin, C.-H. Yan and G.-X. Xu, From Cubane to Supercubane: The Design, Synthesis, and Structure of a Three-Dimensional Open Framework Based on a Ln_4O_4 Cluster, *Angew Chem., Int. Ed.*, 2000, **39**, 3644-3646. DOI:10.1002/1521-3757; (j) H. Ke, P. Gamez, L. Zhao, G.-F. Xu, S. Xue and J. Tang, Magnetic Properties of Dysprosium Cubanes Dictated by the M−O−M Angles of the [$Dy_4(\mu_3$-$OH)_4$] Core, *Inorg. Chem.*, 2010, **49**, 7549-7557. DOI: 10.1021/ic101057e.

22. S. Alvarez, P. Alemany, D. Casanova, J. Cirera, M. Llunell and D. Avnir, Shape maps and polyhedral interconversion paths in transition metal chemistry, *Coord. Chem. Rev*., 2005, **249**, 1693–1708. DOI: 10.1016/j.ccr.2005.03.031.

23. (a) J. Goura, E. Colacio, J. M. Herrera, E. A. Suturina, I. Kuprov, Y. Lan, W. Wernsdorfer and V. Chandrasekhar, Heterometallic Zn_3Ln_3 Ensembles Containing (μ_6-CO_3) Ligand and Triangular Disposition of Ln^{3+} ions: Analysis of Single-Molecule Toroic (SMT) and Single-Molecule Magnet (SMM) Behavior, *Chem. Eur. J.*, 2017, **23**, 16621-16636. DOI:10.1002/chem.201703842; (b) R. Jia, H.-F. Li, P. Chen, T. Gao, W.-B. Sun, G.-M. Lia and P.-F. Yan, Synthesis, structure, and tunable white light emission of heteronuclear Zn_2Ln_2 arrays using a zinc complex as ligand, *CrystEngComm.*, 2016, 18, 917–923. DOI: 10.1039/C5CE02228B.

24. E. Cavalli, S. Ruggieri, S. Mizzoni, C. Nardon, M. Bettinelli and F. Piccinelli, NIR-emission from Yb(III)- and Nd(III)-based complexes in the solid state sensitized by a ligand system absorbing in a broad UV and visible spectral window, *Results in Chemistry*, 2022, **4**, 100388, DOI: 10.1016/j.rechem.2022.100388.

25. (a) A. J. Calahorro, D. Fairen-Jiménez, A. Salinas-Castillo, M. E. López-Viseras and A. Rodríguez-Diéguez, Novel 3D lanthanum oxalate metal-organic-framework: Synthetic, structural, luminescence and adsorption properties, *Polyhedron*, 2013, **52**, 315-320. DOI: 10.1016/j.poly.2012.09.018; (b) L.-Z. Zhang, W. Gu, B. Li, X. Liu and D.-Z. Liao, $\{[Nd_4(ox)_4(NO_3)_2(OH)_2(H_2O)_2]\cdot 5H_2O\}_n$: A Porous 3D Lanthanide-Based Coordination Polymer with a Special Luminescent Property, *Inorg. Chem.*, 2007, **46**, 622-624. DOI: 10.1021/ic061635n.

26. (a) J. Goura, J. P. S. Walsh, F. Tuna, R. Halder, T. K. Maji and V. Chandrasekhar, P–C Bond Cleavage-Assisted Lanthanide Phosphate Coordination Polymers, *Crystal Growth & Design*, 2015, **15**, 2555-2560. DOI: 10.1021/cg5017005; (b) A. R. Ramya, D. Sharma, S. Natarajan and M. L. P. Reddy, Highly Luminescent and Thermally Stable Lanthanide Coordination Polymers Designed from 4-(Dipyridin-2-yl)aminobenzoate: Efficient Energy

Transfer from Tb^{3+} to Eu^{3+} in a Mixed Lanthanide Coordination Compound, *Inorg. Chem.*, 2012, **51**, 8818-8826. DOI: 10.1021/ic300654e.

27. (a) S. Titos-Padilla, J. Ruiz, J. M. Herrera, E. K. Brechin, W.Wersndorfer, F. Lloret and E. Colacio, Dilution-Triggered SMM Behavior under Zero Field in a Luminescent Zn_2Dy_2 Tetranuclear Complex Incorporating Carbonato-Bridging Ligands Derived from Atmospheric CO_2 Fixation, *Inorg. Chem*., 2013, **52**, 9620−9626. DOI: 10.1021/ic401378k; (b) J. Ruiz, G. Lorusso, M. Evangelisti, E. K. Brechin, S. J. A. Pope and E. Colacio, Closely-Related $Zn^{II}_2Ln^{III}_2$ Complexes (Ln^{III} = Gd, Yb) with Either Magnetic Refrigerant or Luminescent Single-Molecule Magnet Properties, *Inorg. Chem.*, 2014, **53**, 3586–3594. DOI: 10.1021/ic403097s.

28. K. A. Thiakou, V. Nastopoulos, A. Terzis, C. P. Raptopoulou, S. P. Perlepes, Di-2-pyridyl ketone in lanthanide(III) chemistry: Mononuclear and dinuclear erbium(III) complexes, *Polyhedron*, 2006, **25**, 539–549.

29. K. A. Thiakou, V. Bekiari, C. P. Raptopoulou, V. Psycharis, P. Lianos, S. P. Perlepes, Dinuclear lanthanide(III) complexes from the use of di-2-pyridyl ketone: Preparation, structural characterization and spectroscopic studies, *Polyhedron*, 2006, **25**, 2869–2879.

30. S. Dominguez, J. Torres, J. Gonzalez-platas, M. Hummert, H. Schumann, C. Kremer, Thermodynamic stability and crystal structure of lanthanide complexes with di-2-pyridyl ketonek, *J. Coord. Chem*. 2009, **62**, 108–119.

31. H.-S. Wang, Z. Zhang, Y. Chen, Z.i-Q. Pan, Z.-B. Hu, C.-L. Yin, Modulation of the directions of the anisotropic axes of Dy^{III} ions through utilizing two kinds of organic ligands or replacing Dy^{III} ions by Fe^{III} ions, *CrystEngComm*, 2019, **21**, 5429–5439.

32. H.-S. Wang, Q.-Q. Long, C.-L. Yin, Z.-W. Xu, Z.-Q. Pan, Syntheses, crystal structures and magnetic properties of sandglass $Dy^{III}_9$and irregular tetrahedron Dy^{III}_4 complexes, *Polyhedron*, 2018, **141**, 69–76.

33. Li Manni *et al*., The OpenMolcas Web: A Community-Driven Approach to Advancing Computational Chemistry, *J. Chem. Theory Comput., 2023, 19, 6933-6991*. DOI: 10.1021/acs.jctc.3c00182

34. (a) I. Tarannum, S. Moorthy and S. K. Singh, Understanding electrostatics and covalency effects in highly anisotropic organometallic sandwich dysprosium complexes [Dy(C_mR_m)$_2$] (where R = H, SiH_3, CH_3 and m = 4 to 9): a computational perspective, *Dalton Trans.,* 2023*,* **52***,* 15576-15589. DOI: 10.1039/D3DT01646C. (b) K. Kumari, S. Moorthy and S. K. Singh, Single-ion magnet behaviour in highly axial lanthanide mononitrides encapsulated in boron nitride nanotubes: a quantum chemical investigation. *Dalton Trans*., 2025, **DOI:10.1039/D4DT03311F**. (c) P. Kalita, N. Ahmed, S. Moorthy, V. Béreau, A. K. Bar, P. Kumar, P. Nayak, J.-P. Sutter, S. K. Singh and V. Chandrasekhar, Slow magnetic relaxation in a homoaxially phosphine oxide coordinated pentagonal bipyramidal Dy(III) complex. *Dalton Trans*., 2023, **52**, 2804-2815. DOI:10.1039/D2DT03789K. (d) S. Saha, I. Tarannum, P. PalRaktim Datta, S. Bala, A. Ghosh, S. K. Singh and R. Mondal, Electrical–Magnetic Properties of Solvent-Induced Di- and Hexanuclear Lanthanide Complexes Based on an Unorthodox N-Rich Ligand. *Cryst. Growth Des*., 2025, **25**, 624–638, DOI: 10.1021/acs.cgd.4c01378. (e) S. Roy, P. Shukla, N. Ahmed, M.-H. Du, I. Tarannum, X.-J. Kong, T. Gupta, S. K. Singh and S. Das, Interplay between anisotropy and magnetic exchange to modulate the magnetic relaxation behaviours of phenoxo bridged Dy_2 dimers with axial β-diketonate co-ligands. *Dalton Trans*., 2022, **51**, 18187-18202. DOI: 10.1039/D2DT03117E.

35. (a) L. F. Chibotaru and L. Ungur, Ab initio calculation of anisotropic magnetic properties of complexes. I. Unique definition of pseudospin Hamiltonians and their derivation. *J. Chem. Phys*. 2012, **137**, 064112. DOI: 10.1063/1.4739763. (b) W. Zhang, A. Muhtadi, N. Iwahara, L. Ungur and L. F. Chibotaru. Magnetic Anisotropy in Divalent Lanthanide Compounds, *Angew. Chem. Int. Ed*. 2020, **59**, 12720. DOI: 10.1002/anie.202003399. (c) M. Li, H. Wu, Z. Xia, L.

Ungur, D. Liu, L. F. Chibotaru, H. Ke, S. Chen, and S. Gao, An Inconspicuous Six-Coordinate Neutral Dy^{III} Single-Ion Magnet with Remarkable Magnetic Anisotropy and Stability. *Inorg. Chem.* 2020, **59**, 10, 7158–7166. DOI: 10.1021/acs.inorgchem.0c00616.

View Article Online
DOI: 10.1039/D4DT02976C

Data availability

All the data are available in the main manuscript or in the ESI.

Electronic supplementary information (ESI) available: Figures and tabulated bond angles/lengths for all compounds. IR, Photoluminescent spectrums, *Ac* susceptibility measurements. Single-crystal data[18a-f] and the CIFs have been deposited with CCDC No. **2379210-2379215** for complexes **1**-**6**. Full results of the SHAPE analysis for the Ln(III) centers in **1**-**6** using SHAPE 2.1,[22]. All these theoretical calculations were carried out using the OpenMOLCAS code.[33]